Article

Experimental Analysis of Rotor Blade Noise in Edgewise Turbulence

Nur Syafiqah Jamaluddin [1,*] ![ORCID], Alper Celik [1,2] ![ORCID], Kabilan Baskaran [1,3], Djamel Rezgui [1] ![ORCID] and Mahdi Azarpeyvand [1]

1   Department of Aerospace Engineering, University of Bristol, Bristol BS8 1TH, UK;
    alper.celik@swansea.ac.uk (A.C.); kabilan@iitism.ac.in (K.B.); djamel.rezgui@bristol.ac.uk (D.R.);
    m.azarpeyvand@bristol.ac.uk (M.A.)
2   Department of Aerospace Engineering, Swansea University, Swansea SA1 8EN, UK
3   Department of Mechanical Engineering, Indian Institute of Technology (ISM), Dhanbad 826004, India
*   Correspondence: syafiqah.jamaluddin@bristol.ac.uk

Abstract: This paper presents an experimental investigation into the effects of turbulence ingestion on the aerodynamic noise characteristics of rotor blades in edgewise flight. A small-scaled, two-bladed rotor was used in the study. The test utilised two turbulence-generating grids, to generate turbulence inflows with different characteristics, and to compare them to the baseline configuration of the laminar inflow. The experiments were set at forwarding edgewise flight configuration, with freestream inflow velocity ranging from 10 m/s to 22 m/s. Simultaneous measurements of far-field acoustic pressure and load were conducted, along with a separate flow measurement using particle image velocimetry. The acoustic spectra demonstrated a larger contribution to the tonal noise radiation at blade passing frequency, and to the broadband noise radiation at the mid-frequency domain, due to turbulence ingestion. However, the broadband responses in the high-frequency domain were comparable between the tested laminar and turbulence inflow cases, with similar broadband humps featuring in the acoustic spectra. The directivity patterns of the overall sound pressure level showed that the noise radiation was lowest near the plane of rotation, and highest downstream. Turbulence ingestion effects could also be seen in the elevated noise levels throughout the observation positions for the grid inflow cases, particularly at larger advance ratios.

Keywords: rotor noise; turbulence ingestion; experimental aeroacoustics; edgewise flight; PIV measurement

1. Introduction

The concept of urban air mobility (UAM) technology as a modern air transportation system is set to become a reality in the near future. This technological advancement has driven significant efforts to understand some of the challenging aspects of these novel vehicle designs. Propellers or rotor blades are one of the vital components used to power UAM technologies, and offer many potential benefits [1]. Various mathematical models have been developed to aid in the future prediction of unknowns associated with rotor blades in UAM applications; hence, it is essential to achieve experimental data to assist in the validation of these predictive models [2]. With the ever-increasing complexity in the design of UAM, the development of low-noise rotor systems continues to be an essential topic of scientific interest. While many studies have been undertaken on rotor noise, such as can be found in [3–15], it is noteworthy that a considerable number of these investigations have not adequately emphasised or sufficiently addressed the impacts of ingesting turbulent flows.

For UAM to provide efficient mobility in urban landscapes, operation in a turbulent flow field has become ubiquitous. The wind and turbulence within the urban boundary layer, induced by wind interaction with the integral components—such as buildings and trees—in the urban landscape, may have influenced the rise in drag, mean wind, and turbulence. The intensity of turbulence in urban or hilly terrain areas is about twice that of

rural sites, due to greater surface roughness, significant directional changes in wind speed, and more extensive thermal heating [16].

Integrated systems of rotary and fixed-wing vehicles are commonly used in UAM design to eliminate the need of a long runway for take-off and landing. The tilt-rotor system is an example of such functionality. The tilt-rotor system utilises a set of rotor blades in non-axial inflow operations, to generate vectored thrust, allowing the vehicle to transition from rotorcraft to fixed-wing aircraft mode. During this transition, the flow field surrounding the rotor becomes more complicated, resulting in intricate aerodynamic interactions between the airflow and the rotor blade surfaces. One of the prevalent attributes of a rotor blade in edgewise flights is the unsteady pressure field, in which asymmetric interactions occur on both the advancing and retreating sides [17]. In edgewise flight, rotor blades perceive both forwarding velocity and angular velocity components, owing to to forward movement and the blade's rotation, respectively. The forward speed increases the relative velocity of the blade on the advancing side, while decreasing it on the retreating side of the blade. As a result, the rotor disc faces a highly non-uniform inflow, which eventually fluctuates the loading distribution over both advancing and retreating sides of the blade [18].

As a blade passes through a tip vortex or unsteady wake generated by the preceding blades or turbulent inflow, blade vortex interaction (BVI) occurs. BVI refers to the phenomenon that occurs when vortex structures, either existing in the approaching flow or trailing from the tip or trailing edge of a preceding blade, directly strike the following blades during the propeller's rotation. This interaction results in an acoustic signature consisting of high-amplitude tonal noise that repeats at the harmonics of the blade passing frequency [19]. This impulsive acoustic signature generated by the blades can lead to significant aerodynamic loading and noise problems [20]. Critical parameters, such as the air load, and the blade tip vortex structures and their trajectories, have been found, in the existing literature, to be the key control factors in attenuating rotor blade–vortex interaction noise and vibration [21].

Turbulence flow can be characterised by its length scale, timescale, intensity, and spectral content. Among these parameters, the impact of turbulence intensity on noise levels is notably significant when interacting with rotating blades, as observed by Scharpf and Mueller [22]. Further, Sevik conducted experimental studies on the sound radiation of a rotating propeller subjected to turbulence ingestion [23]. In this study, the author identified that turbulence in the approach stream is a primary contributor to broadband sound radiation from rotating machinery. According to the findings, the broadband sound power spectrum is dependent on several factors, including the turbulence level, characteristic timescale, and characteristic length scales.

The sound pressure field of rotating blades in free space is an acoustic phenomenon that can be related to and predicted by the forces acting on the blade. The pressure distribution around the propeller and rotor blades determines the sectional lift and drag force generated on the blade's surface, which influence the distribution of acoustic pressure, and the resulting sound radiating into the far field. However, accurate predictions of aeroacoustic performance based on the blade's loading conditions are rather challenging, because the flow surrounding a rotating system is inherently non-linear, unsteady and turbulent [24]. Previous theoretical investigations have proposed that a radiated sound pressure field can be analysed by replacing the distribution of normal pressure caused by blade loadings over the blade surfaces with a distribution of acoustic pressure doublets acting at the propeller disk [25]. This indicates that the acoustic signatures of rotating blades vary, depending on the loading condition (i.e., thrust and torque), and are unique according to the flow condition that each blades encounter. At a low angle of attack, or steady horizontal flight, the generated noise source can be modelled with steady loading conditions. On the other hand, at low tip speed or during take-off and landing, the noise generated is due to the aerodynamic interactions caused by the unsteady loading conditions. The unsteady loading of the blade leads to the development of wake vortices

that convect to the downstream, resulting in periodic blade–vortex interactions at every blade revolution [26].

The present study aimed to support these goals by evaluating the variations in the acoustics and flow field signatures of an isolated small-scaled rotor in turbulent inflows. For brevity, the present work only focused on the non-tilting operation, which features a level edgewise flight operation, with the blade's rotational axis perpendicular to the airstream. The paper compares experimental results of the noise characteristics of propellers operating in laminar and turbulent inflows. The laminar inflow case was performed using the wind tunnel's default working condition, where the airflow is not forced through any turbulence grid when exiting the nozzle, thus producing a clean and smooth flow. The measurements were also performed under grid-generated turbulent inflows, to address the effects of turbulence ingestion and the variations in the turbulent structure sizes. This paper is organised as follows: Section 2 explains the aeroacoustic facility, the experimental rig, and the techniques used; Section 3 provides the results of the experiments in three main parts, which are the aerodynamics and aeroacoustics performance, as well as the characteristics of flow field surrounding the rotor blade; Section 4 reports the conclusion of this manuscript.

2. Experimental Set-Up and Procedures

A series of wind tunnel tests, of an electrically two-bladed rotor in non-axial or edgewise flow, were conducted in an anechoic chamber. The tests were conducted at varying advance ratio operations under three inflow conditions, i.e., laminar inflow and two turbulent inflows, which were generated by passive turbulence grids positioned inside the contraction nozzle of the facility: Grid A and Grid B. Two far-field microphone arrays were used simultaneously to record the acoustic data, namely, the top and side arrays, which were installed above and on the side of the rotor disc, respectively, as outlined in Figure 1. The flow field measurement was performed using the particle mage velocimetry (PIV) technique to compute the statistical time-averaged turbulent flow quantities over the y-z plane. The test rig set-up used in the experiment and the details of the test facility are explained in Section 2.1 and Section 2.2, respectively.

2.1. Test Rig

An isolated rotor configuration, immersed in a turbulent flow, was constructed for the present study. The rotor blade was positioned in the middle of the open jet nozzle, approximately 600 mm downstream of the nozzle exit. Figure 1 illustrates the test rig layout and positioning in the anechoic chamber, the location of the top and side microphone arrays, and the definition of grid dimension employed in the current work.

A two-bladed, 12-inch-diameter rotor blade with a fixed geometric pitch of 4 inches was used in this study, which corresponded to a blade pitch-to-diameter ratio of $P/D = 0.33$. The chord and twist distributions of the blade are shown in Figure 2, as well as the airfoil shape, which was similar to Clark-Y airfoils. The rotor blade was driven by a T-Motor Antigravity MN4006 brushless motor with a diameter of 44.35 mm and a maximum power of 420 W. The motor speed was controlled by a Robotbird 100 A pro electronic speed controller. The set-up was powered by a DC bench power supply, regulated up to a maximum of 25 V. The electrical current was measured at the power supply, as the throttle setting of the ESC was varied to change the speed of the motor. The blade rotation speed was determined by detecting the electrical pulse signal from one of the three wires of the brushless DC motor, taking into account the 24 poles of the motor. The rotor speed was also inspected, using a digital optical Laser tachometer DT-2234C+.
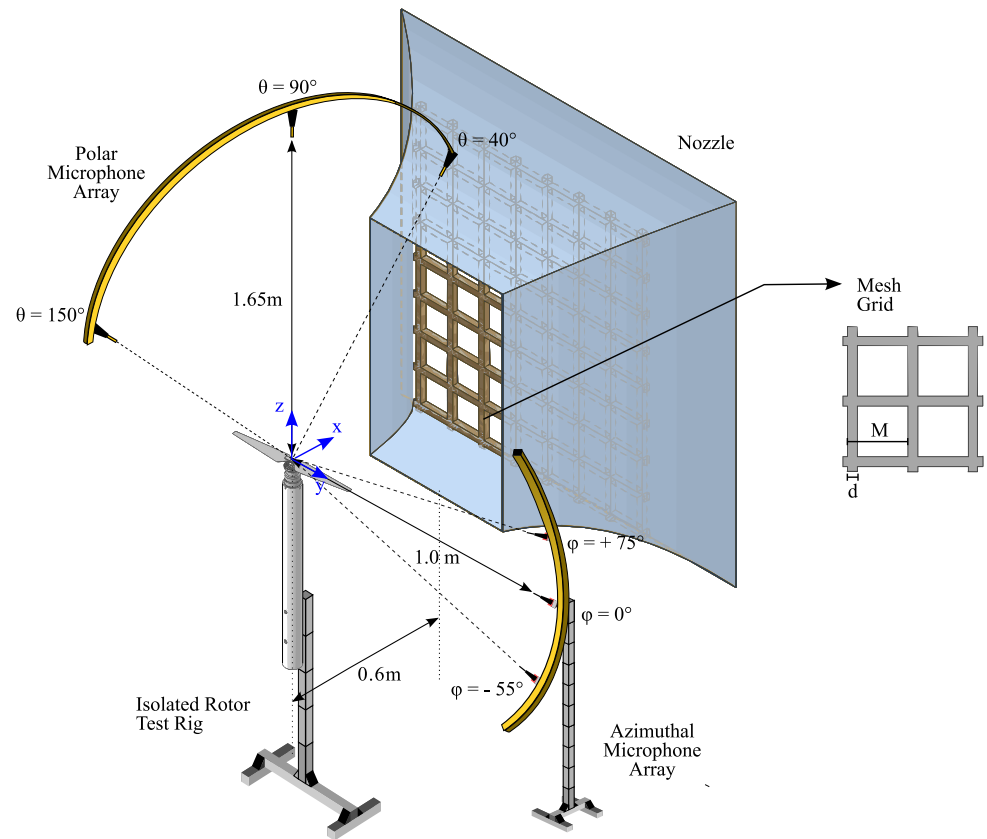
Figure 1. Schematic diagram of the contraction nozzle with turbulence grid in position, the microphone arrays positioning, the isolated rotor test rig, and the definition of grid dimension.
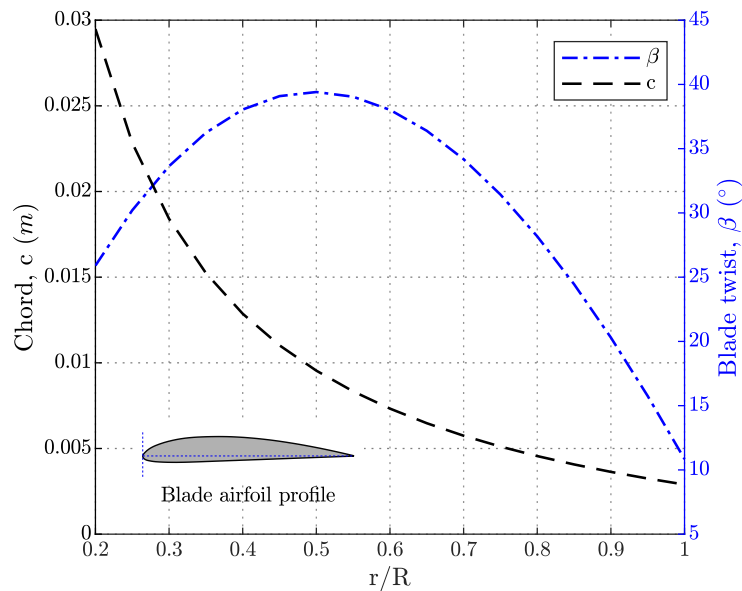

Figure 2. Chord and twist distribution along the blade span. $D \times P = 12'' \times 4''$.

2.2. Measurement Apparatus and Procedures

The experiments were performed in the University of Bristol aeroacoustics facility: an open jet, temperature-controlled, close-circuit anechoic wind tunnel. The contraction nozzle exit was 0.5 m in width and 0.775 m in height, allowing a steady operation from 5 m/s to 40 m/s, with an average turbulence intensity level of less than 0.2%. The facility comprised a large anechoic chamber that was 7.9 m long, 5 m wide, and 4.6 m high, with a

cut-off frequency of 160 Hz. For a more detailed description of the facility, the reader is referred to Mayer et al. [27].

The aerodynamic loading data were collected using an ATI Mini40E 6-axis load cell. The load cell transducer was calibrated by the manufacturer to give a measurement uncertainty with a 95% confidence level. The load measurements were performed for a duration of 16 seconds, and at a sampling rate of 2^{15} Hz. The acoustics measurements were performed using 37 units of ¼ inch-diameter GRAS Sound and Vibration model 40PL microphones, which have an upper limit of 142 dB, and cover a frequency range between 10 Hz to 20 kHz. These microphones were installed on a far-field top plane and side plane arc, allowing noise measurement between the polar angle of $\theta = 40°$ to $150°$, and the azimuthal angles between $\phi = +75°$ and $-55°$, respectively. The polar microphone array was located at a radial distance of 1.65 m above the rotor's plane of rotation, while the azimuthal microphones were installed on the rotor's side plane, at a distance of 1.0 m, measured from the rotor's hub. This configuration correlated to a distance of approximately $5D$ for the top array, and $3D$ for the side array, with D being the rotor diameter. In the study of wave propagation, including sound waves, the far-field region is commonly considered to begin at a distance from the sound source greater than two times its maximum dimension divided by the wavelength of the sound [28]. Given the dimensions of the rotor, and the frequencies of interest to the present study, the microphone placements are considered to be within the far-field region. A National Instruments PXIe-1082 data acquisition system was used, to acquire both loading and far-field noise data. Far-field noise measurements were collected for 16 s, with a sampling rate of 2^{16} Hz.

Two passive turbulence grids were employed, to generate turbulent flows with different turbulence intensities and length scales, in order to measure the effects of homogeneous turbulence ingestion on rotor blade noise. Grids A and B were positioned at $z_g = 1.040$ m, measured from the lip of the nozzle. This positioning corresponded to a contraction ratio of 4.4, which was calculated as the ratio of the grid to the nozzle outlet's area, $C = (A_{Grid})/(A_{Nozzle})$. Initial tests were conducted, to determine the nominal turbulence characteristics of each grid by Bowen et al. [29]. The results indicated an near-isotropic flow characteristic for the grid-generated turbulence, following the good curve fittings between the power spectral density of the velocity fluctuations of the tested grids and the von Kármán spectrum.

These grids were manufactured from MDF sheets that were laser-cut using a Trotec SP500 CO2 laser engraver and are measured 1.305 m in width and height. The grid was constructed in two parts that were coupled using several butterfly hinges positioned at the back of the grid relative to the flow. This approach allows the grid to fit through the nozzle and minimises possible influence on turbulence generation. Grids A and B differed in geometric properties, such as mesh size (M) and bar diameter (d), resulting in almost double the amount of turbulence intensity for Grid B when compared to Grid A. Table 1 describes the size of the grids, and the details of the turbulent flow properties, as measured at the nozzle. For a more detailed description of the grid turbulence characterisation, the reader is referred to Bowen et al. [29].

Table 1. The geometrical and turbulent flow properties generated by the corresponding grid, measured at the nozzle in the wind tunnel.

	Diameter, d (mm)	Mesh, M (mm)	Solidity Factor, (σ)	Turbulence Intensity, TI (%)	Length Scale, λ (mm)
Grid A	19	100	0.35	4.9	13
Grid B	45	233	0.35	10.1	19

A particle image velocimetry (PIV) measurement was performed, to compute the statistical time-averaged turbulent flow quantities over the x-z plane. A FlowSense 4 MP CCD camera was installed perpendicular to the laser sheet adjacent to the rotor blade test rig. The experiment was carried out by capturing image pairs with a resolution of 2072 × 2072

pixels for each case at approximately the middle of the rotor blade's plane of rotation. The measurements were made for a field view of 310 mm × 310 mm, covering around the entire length of the rotor blade. To obtain the maximum quantity of particles in the interrogation window, a dual-cavity laser of 200 mJ Nd:YAG, with a wavelength of 532 nm, was used, to generate a 1 mm laser sheet thickness, with a time interval between each snapshot varied with velocity and repetition rate of 15 Hz. A LaVision GmbH diethylhexyl sebacate seeding, with a particle size of approximately 0.3 to 1 μm, was used to seed the flow. In order to ensure convergence, 1200 image pairs were captured, to obtain instantaneous velocity fields, which were then averaged to obtain a time-averaged velocity field for each case.

3. Results and Discussions

3.1. Aerodynamic Loading Performance

In the present work, the rotor blade was configured in an edgewise inflow condition relative to the air stream, similar to conventional helicopters in level forward flight operations. The mean inflow velocity, U_∞, was set to a range from 10 m/s to 22 m/s, while the rotation speed, Ω, was maintained at a constant rotational speed of 5500 rpm. This setting corresponded to an advance ratio μ, between 0.1 to 0.25, which was calculated as the ratio between the freestream velocity and the tip velocity $U_\infty/\Omega R$, where R was the blade radius. Under conditions of zero wind speed, the rotational speed setting corresponded to a tip Mach number of 0.26 for the tested blade size. The edgewise rotor experienced two different behaviours in every rotation, depending on the blade's azimuthal position or velocity vector relative to the freestream. The relative air velocity normal to the blade was maximum at the advancing blade side, and minimum at the retreating blade side. This velocity differential would generate more lift on the advancing side than on the retreating side, because the blades were rigidly connected to the hub, and there was no flapping hinge. In the present work, the aerodynamic performance was evaluated using the loading data measured from the load cell transducer mounted behind the motor. The data corresponded to the total load generated along the blade's rotational axis, comprised of the thrust (T) force acting in the normal direction against the plane of rotation and the angular force torque (Q).

The measured averaged thrust and torque forces are plotted in Figure 3 for different inflow velocities at a constant rotational speed. The results present the variation of loading generated when tested in laminar and grid inflow conditions. The standard deviation errors are also shown for repeated data measurements. The results indicate that ingesting both the grid turbulences slightly increased the magnitude of thrust generated by the rotor blade at less torque than in laminar inflow condition at any given inflow velocity. This trend suggests that an additional radial force component was exerted and transmitted to the rotor shaft, due to the ingestion of an unsteady and turbulent flow field [30].

The aerodynamic coefficients were calculated from the measured loading data, in terms of coefficient of thrust (C_T) and coefficient of power (C_P), which were calculated as

$$C_T = \frac{T}{\rho(R\Omega)^2 A},$$

$$C_Q = C_P = \frac{\Omega Q}{\rho(R\Omega)^3 A},$$

where A was the area of the rotor disc, Ω was the propeller's rotational speed in rad/s, and ρ was the air density.

The results in Figure 4a demonstrate that at a constant rotational speed, thrust increased with inflow velocity irrespective of the inflow condition. Meanwhile, the power required by the rotor blade, to generate the same amount of lift as the flight speed, increased. This trend suggests a relatively advantageous operation at a higher advance ratio, as indicated by the plots of the power coefficient in Figure 4b. Notably, in laminar inflow, the rotor blade consumed relatively more power at $\mu \geq 0.15$, while producing slightly less

thrust than in the Grid A and Grid B turbulent inflows: the differences, however, can be considered negligible.
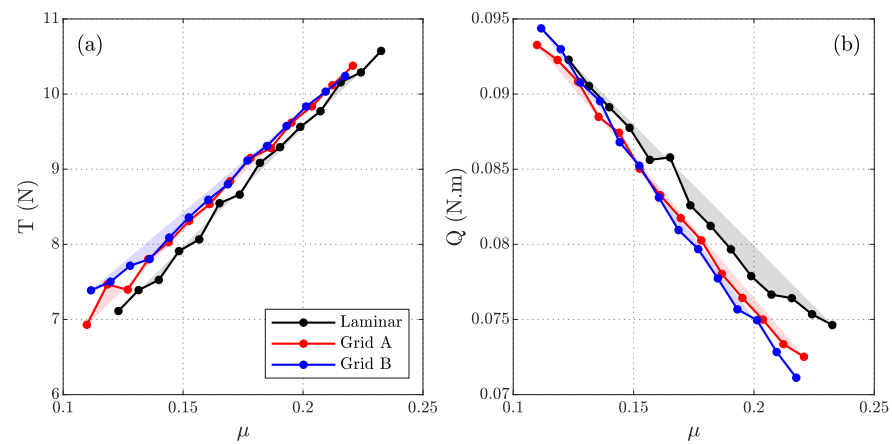

Figure 3. The aerodynamic loading of (**a**) thrust, and (**b**) torque measured for rotor operating in laminar (solid black line), Grid A (solid red line), and Grid B (solid blue line) at 5000 rpm rotation speed. The shaded areas show the standard deviation error.
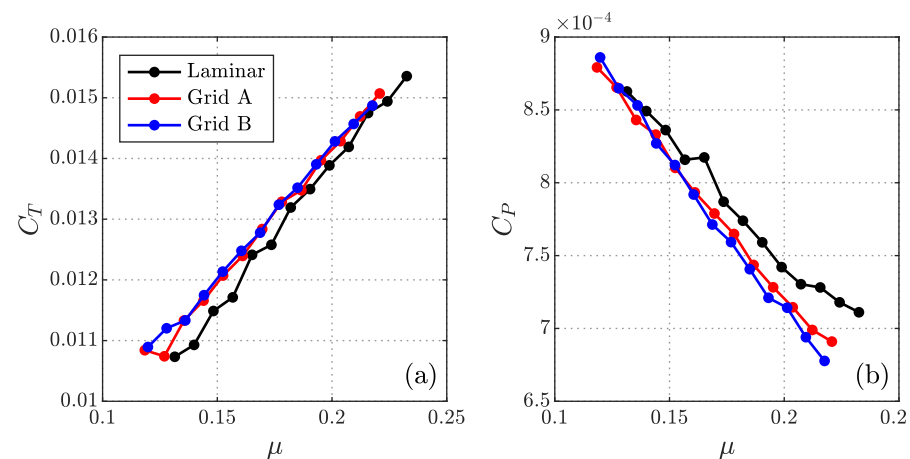

Figure 4. The calculated aerodynamic parameters, (**a**) coefficient of thrust, and (**b**) coefficient of power, for rotor operating in laminar (solid black line), Grid A (solid blue line), and Grid B (solid red line) at 5000 rpm rotation speed.

3.2. Far-Field Noise Spectrum

Propeller noise is classified into harmonic tonal noise and broadband noise [26,31]. For this section, power spectral analyses were used, to characterise the aeroacoustics feature of the rotor blade under various turbulent inflow and operating conditions (blade rotational speed and streamwise inflow speed), using far-field microphone signals. The noise radiations of the energy content in the spectrum were also analysed, to reveal its directivity feature. The time-averaged flow field analyses revealed insights into the flow properties across the blade disc, and its associative links to the tested inflow turbulence.

The acoustics spectra are presented in this section, to characterise the frequency–energy content in the radiated noise. The energy content in the noise spectra are presented in terms of the power spectral density (PSD) of the spectrum of noise, which was calculated using

$$PSD = 10\log_{10}\left(\phi_{pp}/p_{ref}^2\right),$$

where ϕ_{pp} was the PSD of the measured acoustic pressure, and p_{ref} was the conventional reference pressure of 20 µPa. Figure 5 shows the top plane acoustic spectrum obtained from

the polar microphone arrays, which were located above the plane of rotation of the rotor. The laminar inflow data were compared to the Grid A and B turbulent inflows for three advance ratio operating conditions: 0.14, 0.18, and 0.3. These PSD data were measured at a fixed rotational speed of 5500 rpm. The presented results were measured from the polar microphone position of $\theta = 90°$, perpendicular to the upstream direction. The results at the fundamental blade pass frequency ($f/BPF = 1$) were magnified, and presented on the side of a larger frequency envelope, ranging between 100 Hz and 30 kHz, for the comparison.
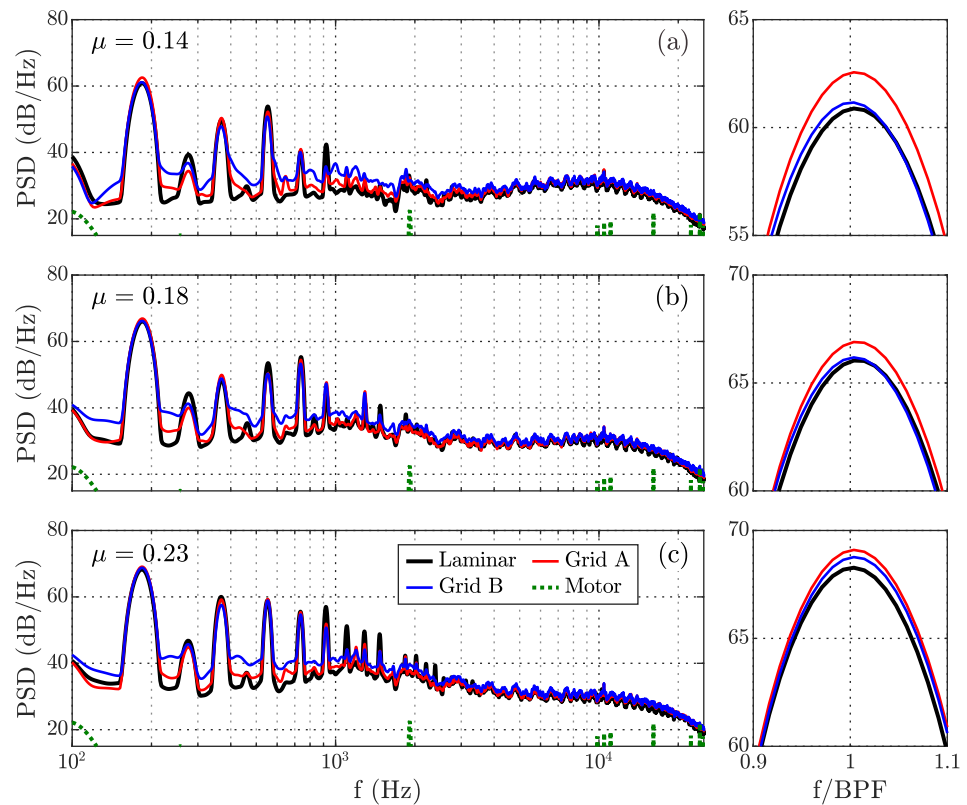
Figure 5. The power density spectrum at the top plane array for a polar observation position of $\theta = 90°$, presented in the frequency domain for an advance ratio setting of (**a**) $\mu = 0.14$, (**b**) $\mu = 0.18$, and (**c**) $\mu = 0.23$. The spectra of the motor-only noise for the same rotational speed are also shown.

It can be seen that the results of the laminar, Grid A, and Grid B inflows compared reasonably well, in terms of their tonal and broadband noise content, regardless of the rotor's operating advance ratio. However, the multiples of tonal frequencies due to BPF increased at a higher advance ratio. This trend is evident from the total number of high-amplitude tonal peaks that can be seen in the lower-to-mid-frequency region, between 100 and 10,000 Hz, where BPF multiples with amplitudes above 50 dB/Hz increased from three harmonics at $\mu = 0.14$ to around seven harmonics at $\mu = 0.23$. In a closer look at the fundamental BPF ($f = 183$ Hz), the Grid A results demonstrated the highest amplitude at all tested advance ratio operations. Meanwhile, the laminar and Grid B inflows results were noticeably similar, at $\mu = 0.14$ and 0.18. Nevertheless, at $\mu = 0.23$, a distinct increase in the BPF amplitude for the Grid B turbulence case can be seen, compared to the laminar inflow results. This trend suggests potential noise source mechanisms related to the rotor operating conditions, intensifying the effects of turbulence ingestions, particularly for the fundamental blade pass frequency of the tonal noise.

The acoustic spectra of the same rotor operational settings measured from the side plane of the rotor disc are shown in Figure 6. The results represent an azimuthal observation position of $\phi = 0°$, as indicated in Figure 1. It is important to note that a distance correction factor was applied to the data, to compare both microphone arrays (top and side), assuming

spherical wave propagation in a free field. Significant differences can be seen, for the first harmonic tonal noise, between the laminar inflow and the grid turbulence cases. The Grid A and B cases recorded an increase of blade pass frequency tones of approximately 8 dB/Hz, relative to the laminar inflow for the operational range between $\mu = 0.14$ and 0.23. It can also be seen that the side plane acoustic spectrum exhibited features that contained higher harmonics tonal peaks that were more spread out over the low-frequency range (100–1000 Hz) at all tested advance ratios, as compared to the aforementioned top plane spectrum.

It is important to note that the motor-only noise (dashed green line) depicted a significant energy content at around 10.3 kHz, with a magnitude larger than 50 dB/Hz. This high-frequency noise component appeared in the vicinity of approximately $f = 18 \times \Omega$, which may have been related to the 18 electromagnetic poles of the motor used in the experiment, similarly reported by Baars et al. [32]. This additional energy content from the motor may generate an additional noise source of a similar frequency range for laminar and grid turbulent cases, as seen in the spectrum.
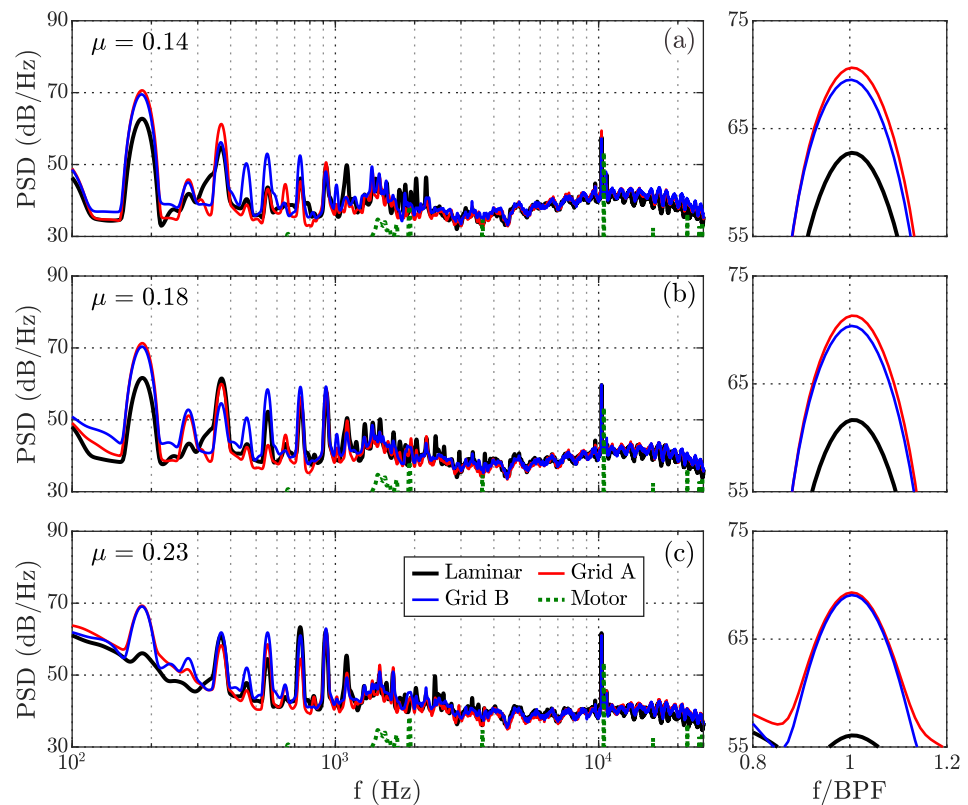

Figure 6. The power spectral density of rotor noise at an azimuthal angle of $\phi = 0°$, presented in the frequency domain for an advance ratio setting of (**a**) $\mu = 0.14$, (**b**) $\mu = 0.18$, and (**c**) $\mu = 0.23$.

3.3. Noise Radiation Directivity

The acoustic energy of the observed rotor noise spectra was investigated over a resolved frequency range, to explore the directivity features over the top and side planes. The noise magnitude is presented in terms of the overall sound pressure level (OASPL), which was calculated by integrating the energy spectrum with respect to frequency using,

$$OASPL = 10 \cdot \log_{10} \left[\frac{\int PSD(f)\,df}{p_{ref}^2} \right],$$

where PSD was the power spectral density of the sound pressure, derived using Welch's method based on unsteady pressure fluctuation [33]. Figures 7 and 8 present the far-field

noise directivities at the polar and streamwise planes, measured from the top and side microphone arrays, respectively. These results were computed using a resolved frequency, f, ranging from 100 Hz to 30 kHz, and are shown for advance ratio operations of 0.14, 0.18, and 0.23 at a fixed rotation speed of 5500 rpm. The noise directivities in the top plane, as shown in Figure 7, resemble a distribution of concentric rings, regardless of the rotor operation setting and inflow conditions. This concentric ring feature was slightly directed downstream from the rotation plane, and may have been related to the tonal noise component associated with loading and the geometrical feature of the blade, as previously seen by Qi et al. [34]. The highest levels of overall sound pressure were observed near the rotation axis, directed towards the wake of the rotor (between $\theta = 80°$ to $110°$). A notable increase in the OASPL can be seen for the Grid A inflow cases, compared to the laminar and Grid B inflows, especially in the downstream observation angles.
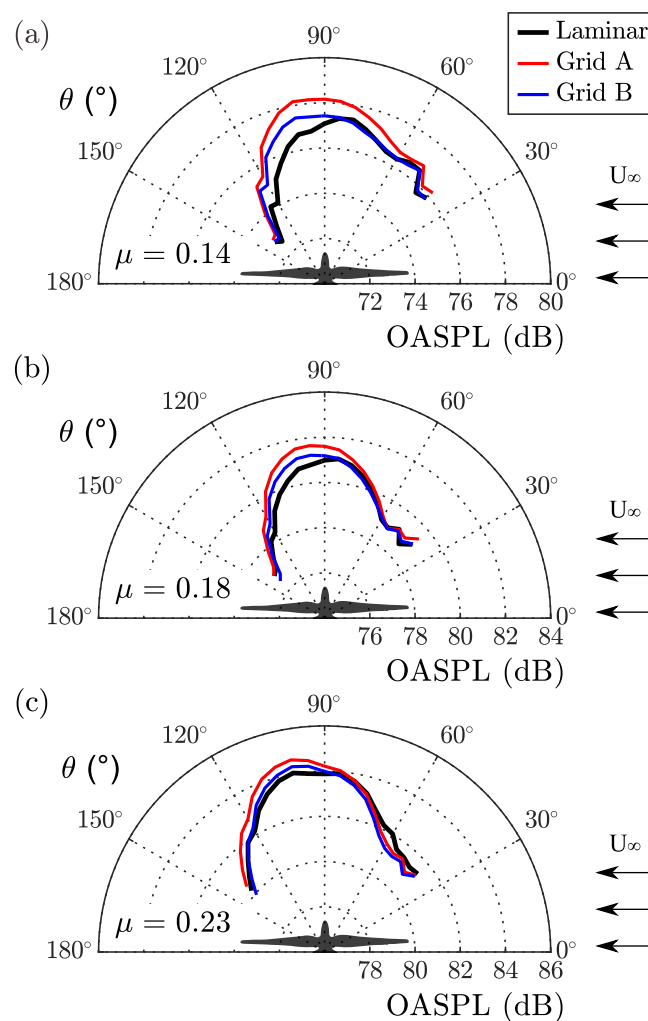

Figure 7. Polar noise directivity in the top plane for rotor blade operating at advance ratio of (**a**) $\mu = 0.14$, (**b**) $\mu = 0.18$, and (**c**) $\mu = 0.23$.

The noise directivities in the side plane, as shown in Figure 8, resembled a cardioid dipole feature, with its centre axis aligned to the rotor's plane of rotation ($\phi = 0°$). Regardless of the inflow conditions, the results exhibited apparent cardioid-shaped directivity trends that were not observed in the top plane, where the minimum levels of noise magnitude were recorded at $\phi = 0°$. A substantial increase in the OASPL could be seen between laminar inflow cases and grid turbulence, especially in the region above the rotor disc (between $\phi = +90°$ and $\phi = 0°$; however, the differences between the two grid cases were insignificant.

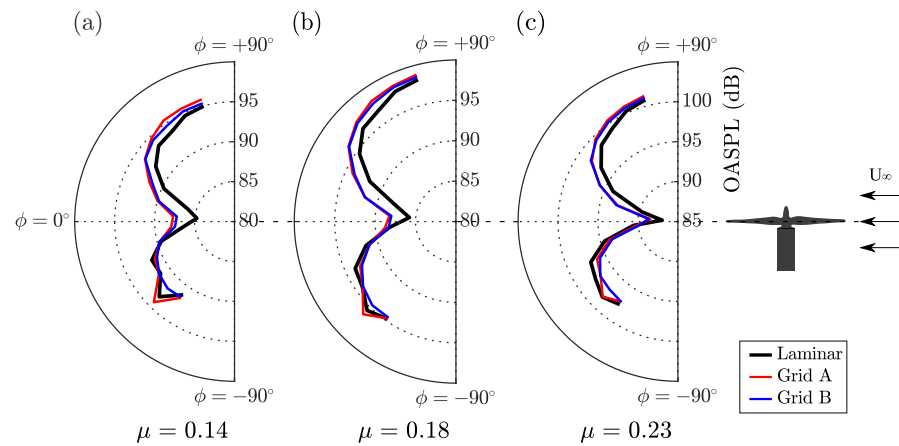**Figure 8.** The noise radiation pattern in the side plane for rotor blade operating at advance ratio of (**a**) $\mu = 0.14$, (**b**) $\mu = 0.18$, and (**c**) $\mu = 0.23$.

The directivities of the tonal noise radiation were also investigated, using a similar OASPL analysis, except that the calculations only considered a smaller domain of low-frequency range. The magnitudes of the sound pressure levels (SPL) of the tonal noise were calculated within a narrowband frequency range of ± 10 Hz of the integer multiples of blade pass frequency. The results are presented in the first-, second-, and third-order harmonics of BPF, corresponding to a resolved frequency range between 173 to 193 Hz, 356 to 376 Hz, and 540 to 560 Hz, respectively.

The polar radiation patterns of harmonic noise on the top plane are presented in Figure 9 for three advancing ratio operations. The noise directivity of the first harmonics of BPF (see Figure 9a) were highly oriented towards the downstream flow region, with maximum levels recorded near the blade rotation axis, which closely resembled the concentric rings directivity trends previously seen in Figure 7. At higher advance ratio operations, the noise magnitudes noticeably increased at all polar angle observation points, regardless of the inflow conditions. The Grid A inflow results exhibited the highest levels of the OASPL, compared to Grid B and laminar inflow, at all tested advance ratios.
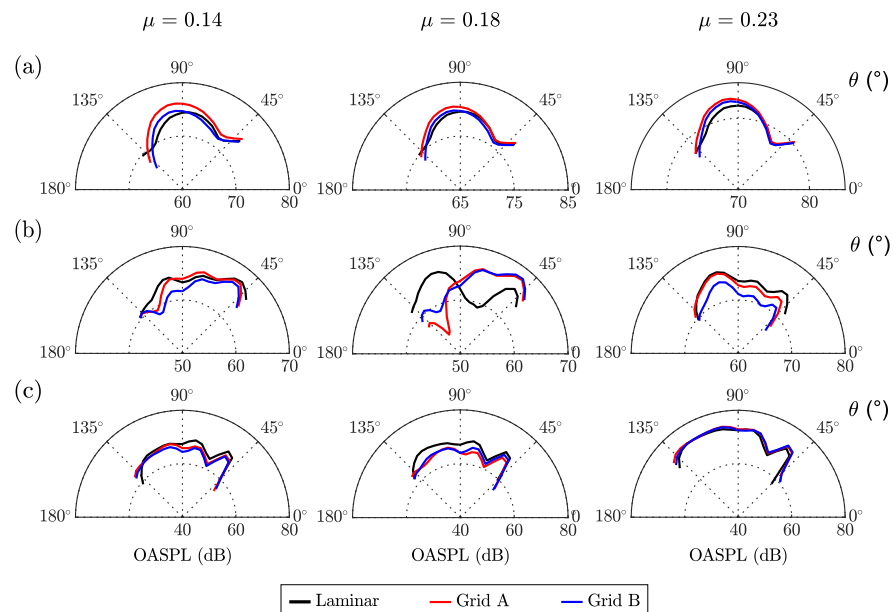

Figure 9. Rotor noise directivity characteristics at top plane for $\mu =$ 0.14, 0.18, and 0.23, over short frequency domain of (**a**) fundamental blade pass frequency, (**b**) second harmonics of BPF, and (**c**) third harmonics of BPF.

The directivity of the second-order harmonics of BPF, as shown in Figure 9b, demonstrated a slight decrease in magnitude, compared to those from the first-order. Meanwhile, its radiation at all tested advance ratios obeyed no real patterns, and exhibited multiple peaks and pits in noise magnitude levels across the observation angles. A further decrease in noise magnitude across all polar angles could be observed for the third-harmonic noise, as presented in Figure 9c. However, for all tested advance ratio operations, the radiation patterns appeared to be more consistent, with an apparent content of major lobes oriented downstream ($\theta = 65°$ to $140°$), and comparatively smaller side lobes upstream ($\theta = 40°$ to $65°$).

Figure 10 presents the radiation directivities of narrowband harmonic noise in the side planes, measured from a range of azimuthal points of observation. The BPF harmonic noise radiation patterns exhibited the expected dipole feature for all tested advance ratios, where the characteristics remained evident in the first-, second-, and third-order harmonics, presented in Figure 10a–c, respectively. The dipolar patterns were mostly centred and aligned to the rotor's plane of rotation, at $\phi = 0°$, and were highly oriented toward the upper region of the rotor disc. The results of the Grid A and B turbulence inflow cases appeared relatively comparable; however, throughout the azimuthal positions, there was a considerable increase in noise magnitude relative to the laminar inflow for the first- and third-order harmonics of BPF.
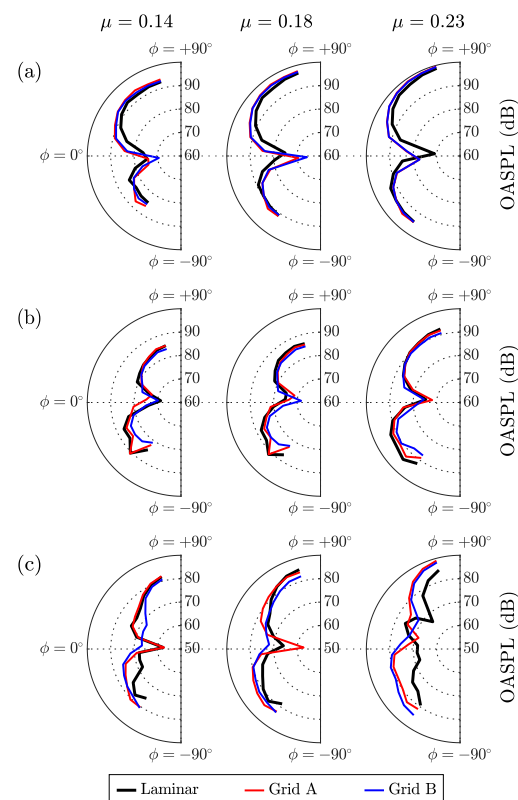

Figure 10. Rotor noise directivity characteristics at the side plane of the rotor for $\mu =$ 0.14, 0.18, and 0.23, over short-frequency domain of (**a**) fundamental blade pass frequency, (**b**) second harmonics of BPF, and (**c**) third harmonics of BPF.

3.4. Time-Averaged Flow Field

To further understand the impact of turbulence ingestion on the wake development, measurements were made with PIV at a flow velocity of $U_\infty = 16$ m/s, and a blade rotation speed of 5500 rpm, corresponding to an advance ratio of $\mu = 0.18$. This section presents the time-averaged flow quantities of the flow field surrounding the blade at both upstream and downstream locations, between $x = -1R$ and $x = +1R$, where R represents the radius of the blade. The measurements were taken on the x-z plane near the hub of the rotor blade,

at the laminar, Grid A, and Grid B inflows. The measurements were made for a field view of 310 mm × 310 mm, which corresponded to a domain of $2R \times 2R$ in the streamwise and vertical directions, as shown schematically in Figure 11. The effects of turbulence ingestion were analysed from the variation of the magnitude of the total velocity (U_{total}) and the mean turbulent kinetic energy (TKE) associated with eddies in the streamwise flow. Due to the structural limitation, the laser sheet was placed at an offset location in the y-axis, by approximately $0.2R$, where $y/R = 0.2$.
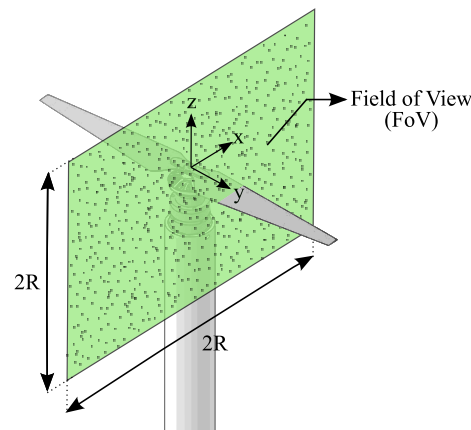
Figure 11. The PIV measurement plane was the x-z plane, with the freestream velocity aligned in the x-axis direction.

The total velocity variation was presented as the normalised, time-averaged inflow velocity (U_{total}/U_∞), where U_{total} was the magnitude of total velocity, and U_∞ was the freestream velocity. Meanwhile, the mean turbulent kinetic energy was calculated as half the sum of the root mean square of the measured velocity components, using

$$TKE = 0.5(\overline{u}^2 + \overline{v}^2),$$

where $\overline{u}$ and $\overline{v}$ were the root mean square values of the vertical and streamwise velocity components, respectively.

Figure 12 illustrates the contour of the time-averaged, normalised total velocity (U_{total}/U_∞) around the rotor disc, with and without turbulence ingestion. The total velocity, U_{total}, was resolved from the streamwise (u) and vertical (v) velocity components in the flow field. The velocity vectors, which were also comprised of the streamwise and vertical velocity components, are presented on top of each contour, to illustrate the evolution in the streamline's direction within the flow field domain. The results show the presence of a distinct velocity gradient across the streamwise plane, indicating that the rotor blade surface was interacting with the flow. It should be noted that these PIV measurements were taken between the tips of the blade: hence, the accelerated flow at the further upstream and downstream locations was indiscernible. The results show that, regardless of the inflow conditions, variations in velocity gradient were evident in two main domains: the first was in the upstream domain above the rotor's streamtube ($z/R > 0$), while the second was downstream, at the wake of the blade ($-1 \leq x/R \leq 0$). The results from the Grid B case, with a larger turbulence length scale, demonstrated a relatively broader area of localised flow acceleration upstream of the streamtube than the laminar and Grid A inflows. Meanwhile, the downstream field near the wake of the blade exhibited a noticeably larger region of accelerated flow during laminar operation, as opposed to both of the grid inflows.
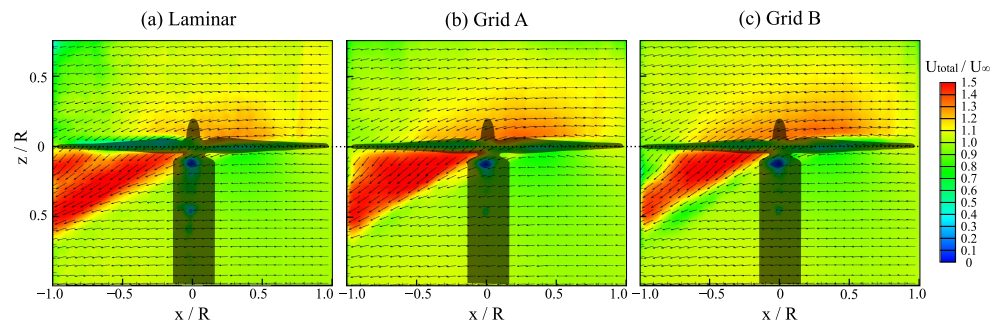
Figure 12. Time-averaged flow contour for normalised total velocity (U_{total}/U_∞) for (**a**) laminar, (**b**) Grid A, and (**c**) Grid B inflow conditions.

In order to better visualise the parametric variations at specific locations in the flow field, statistical turbulent flow quantities were extracted, and computed from the velocity contour. The evolution of velocity profile and development of vortex in the flow field, specifically within the blade disc area, could be assessed by looking into the airflow acceleration and the levels of turbulent kinetic energy in the flow field. The results are presented in Cartesian graphs, as shown in Figures 13 and 14. A total of 10 streamwise locations are included, spanning from the tip of the blade downstream ($x = -1.0R$) to the tip of the blade upstream ($x = +1.0R$), at every increment of $x/R = 0.2$. It should be noted that the rotor's plane of rotation, or the rotor disc, was located at a vertical location of $z/R = 0$, and that the shaded blade areas are included in the results, for illustration.
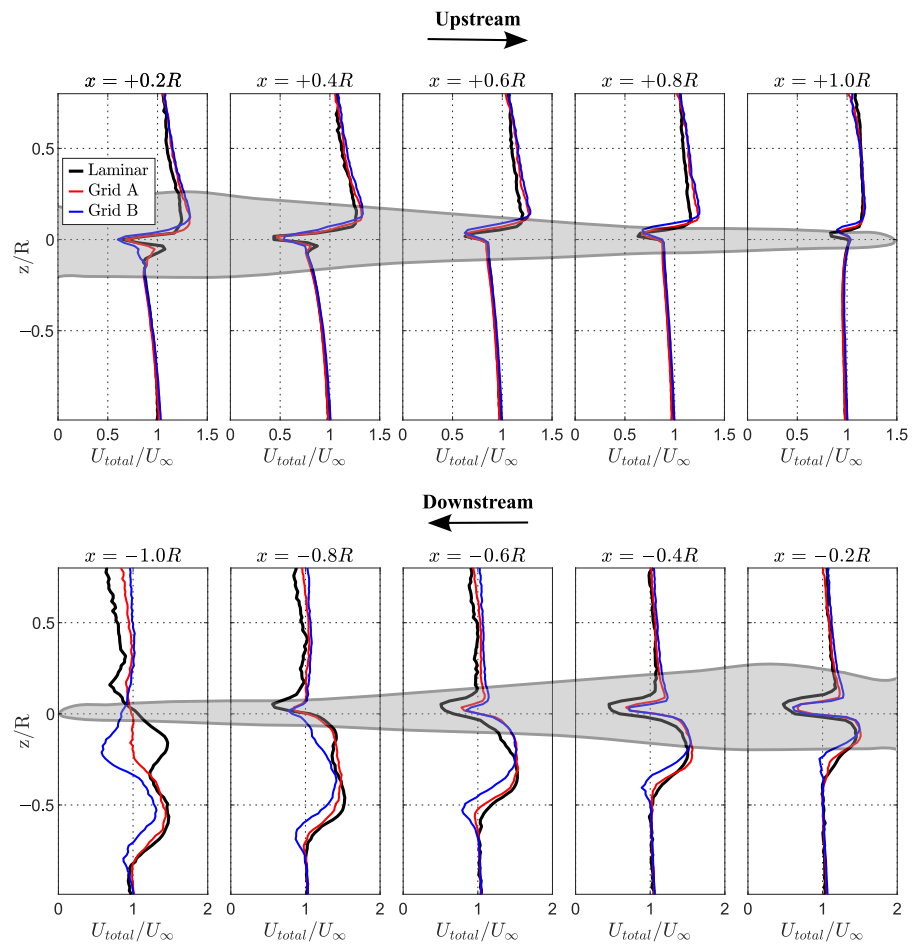

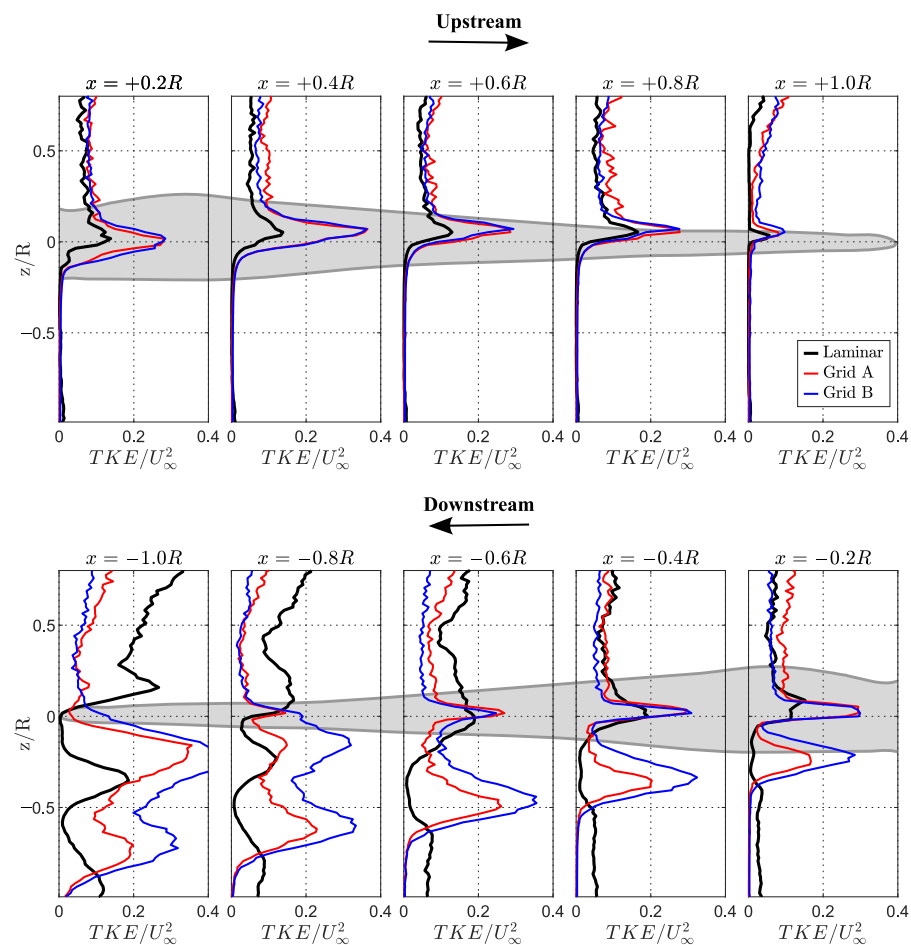**Figure 13.** Distribution of normalised total velocity along the blade disc.

Figure 14. Comparisons of turbulent kinetic energy distribution along the blade disc.

Figure 13 shows the normalised total inflow velocity (U_{total}/U_∞) versus the non-dimensional vertical location (z/R). The results show that the airflow accelerated in the upper region of the streamtube ($z/R > 0$), and peaked at around $z = 0.2R$, just over the blade surface, which was near the rotor's plane of rotation. This characteristic could be seen in the upstream flow region, where the Grid A and B results indicated a noticeable increase in streamwise velocity, compared to the laminar inflow. Meanwhile, the airflow slightly decelerated above the blade's rotation plane, as it travelled further downstream. At the same time, an increasing streamwise flow acceleration was apparent below the plane of rotation ($z/R < 0$). Another interesting observation within this domain was that the Grid B inflow was less accelerated, as opposed to the laminar and Grid A inflows, which appeared to be fairly comparable.

The variation of normalised turbulent kinetic energy TKE/U_∞^2 is presented in Figure 14 against the non-dimensional vertical location, z/R. The results indicate a significant increase in the levels of turbulent kinetic energy across a short domain of $+0.2 < z/R < -0.2R$, which was near the upper and lower regions of the blade disc. It can be seen that both grid inflow results display a significant increase in TKE throughout the upstream blade regions, as opposed to the laminar inflow, which is elongated in the streamwise direction, from $x = +1.0R$ to $+0.2R$. The wake development in the downstream blade regions can be seen in the figure, where the levels of TKE vary progressively in the induced flow field at the wake of the rotor, corresponding to a vertical domain between $x = 0.2$ to $0.8R$. More importantly, the Grid B results in those domains show an increase in TKE of up to 95% compared to the laminar; whereas, in the case of Grid A—which had a smaller turbulence length scale—the TKE increased by approximately half that of Grid B.

The results in Figure 14 also reveal a difference in TKE levels between the laminar and grid cases within the downstream domain from $x = -1R$ to $x = -0.6R$: this discrepancy may be attributed to the energy transfer from the rotating blade to the surrounding fluid. When the rotor operated under laminar inflow conditions, it operated more efficiently, as less energy was used in overcoming drag and turbulence; consequently, more of the input energy could be used to generate lift and thrust, unlike when the rotor was under turbulent inflow conditions. Further analysis of the root mean square (r.m.s) of the velocity fluctuations, in both streamwise and radial directions, showed a notable increase in laminar inflows compared to turbulence inflows within this domain. Although the r.m.s plots are not presented, for brevity, it is important to note that TKE was a function of the r.m.s of the velocity fluctuations in both the streamwise and the radial directions.

4. Conclusions

The effects of turbulence ingestion on the noise characteristics of a two-bladed rotor in edgewise flight operation were examined. The far-field noise spectral characteristics of the propeller were identified at both the polar and the azimuthal observation positions on the top and side planes of the rotor disc. Artificially generated turbulence, using mesh grids, was employed to analyse the rotor–turbulence interactions, using loading, far-field noise, and PIV measurements. The study revealed the considerable influence of turbulence ingestion on the spectral content and directivity characteristics of narrowband tonal noise, which affected the overall sound pressure levels and radiation trends. The data suggest that in a low-to-mid-frequency band, below 1000 Hz, turbulence with a larger length scale, represented by Grid A, increased the tonal noise content more than turbulence with a smaller length scale, represented by Grid B, when compared to the baseline cases of laminar inflow. In contrast, the ingestion of Grid A and B turbulence did not appear to affect the content of high-frequency broadband noise. This observation implies that the broadband noise source mechanism may not have been significantly affected by the turbulence ingestions within the tested operational settings. The OASPL radiation on the top plane was highest in the wake of the rotor in the downstream direction. Meanwhile, on the side plane, the radiation trends were nearly identical over the top and lower regions of the blade disc. The latter trend indicates an apparent cardioid pattern, with its central axis aligned to the plane of rotation. Upon closer examination, the trend in the OASPL radiation closely resembles that of the first-order harmonic tones on both the top and the side planes. The flow field analysis shows that both grids' turbulence contributed significantly to the increase in turbulent kinetic energy in the upstream blade region, especially at the closest proximity to the blade hub, at around $x = +0.4R$. Meanwhile, in the downstream blade region, the Grid B turbulence cases exhibited a significant increase in TKE levels over the lower parts of the blade disc, when compared to the Grid A and laminar cases. A more comprehensive investigation is required, to fully understand the influence of turbulence ingestion on the acoustic response—particularly for identifying the mechanisms behind the noise generation, and their correlation with the flow interaction. Hot-wire measurements could be performed in the wake of the rotor, to gain a better understanding of both the average and spectral characteristics of the flow field. The flow field analysis should also be extended to further upstream and downstream domains, providing insights into the development of turbulent structures, as the flow interacts with the blade and transitions into the wake.

Author Contributions: Conceptualization, N.S.J., D.R. and M.A.; methodology, N.S.J. and A.C.; software, N.S.J. and K.B.; validation, N.S.J. and K.B.; formal analysis, N.S.J., A.C., K.B., D.R. and M.A.; investigation, N.S.J. and A.C.; data curation, N.S.J., A.C. and K.B.; writing—original draft, N.S.J.; writing—review & editing, N.S.J., A.C., K.B., D.R. and M.A.; visualization, N.S.J. and A.C.; supervision, D.R. and M.A.; project administration, D.R. and M.A.; funding acquisition, D.R. and M.A. All authors have read and agreed to the published version of the manuscript.

References

1. Filippone, A.; Barakos, G.N. Rotorcraft systems for urban air mobility: A reality check. *Aeronaut. J.* **2021**, *125*, 3–21. [CrossRef]
2. Rizzi, S.; Huff, D.L.; Boyd, D.D.; Bent, P.; Henderson, B.S.; Pascioni, K.A.; Sargent, D.C.; Josephson, D.L.; Marsan, M.; He, H.; et al. *Urban Air Mobility Noise: Current Practice, Gaps, and Recommendations*; Technical Report 2020-5007433; National Aeronautics and Space Admin Langley Research Center: Hampton, VA, USA, 2020.
3. Sinibaldi, G.; Marino, L. Experimental analysis on the noise of propellers for small UAV. *Appl. Acoust.* **2013**, *74*, 79–88. [CrossRef]
4. Zawodny, N.S.; Boyd, D.D., Jr.; Burley, C.L. Acoustic characterization and prediction of representative, small-scale rotary-wing unmanned aircraft system components. In Proceedings of the AHS 72nd Annual Forum, West Palm Beach, FL, USA, 17–19 May 2016.
5. Zawodny, N.S.; Haskin, H. Small propeller and rotor testing capabilities of the NASA Langley low speed aeroacoustic wind tunnel. In Proceedings of the 23rd AIAA/CEAS Aeroacoustics Conference, Denver, CO, USA, 5–9 June 2017. [CrossRef]
6. Zawodny, N.S.; Haskin, H.; Nark, D.M. Aerodynamic performance and acoustic measurements of a high-lift propeller in an isolated configuration. In Proceedings of the 24th AIAA/CEAS Aeroacoustics Conference, Atlanta, GA, USA, 25–29 June 2018. [CrossRef]
7. Zawodny, N.S.; Boyd, D.D. Investigation of rotor–airframe interaction noise associated with small-scale rotary-wing unmanned aircraft systems. *J. Am. Helicopter Soc.* **2019**, *65*, 1–17. [CrossRef]
8. Tinney, C.E.; Valdez, J. Thrust and acoustic performance of small-scale, coaxial, corotating rotors in hover. *AIAA J.* **2020**, *58*, 1657–1667. [CrossRef]
9. Jamaluddin, N.S.; Celik, A.; Baskaran, K.; Rezgui, D.; Azarpeyvand, M. Aerodynamics and aeroacoustics characterisation of isolated rotor in hover and transition to forward flight. In Proceedings of the 2021 AIAA Aviation Forum, Virtual Event, 2–6 August 2021. [CrossRef]
10. Jamaluddin, N.S.; Celik, A.; Baskaran, K.; Rezgui, D.; Azarpeyvand, M. Aeroacoustic Performance of Propellers in Turbulent Flow. In Proceedings of the 2021 AIAA Aviation Forum, Virtual Event, 2–6 August 2021. [CrossRef]
11. Celik, A.; Jamaluddin, N.S.; Baskaran, K.; Rezgui, D.; Azarpeyvand, M. Aeroacoustic performance of rotors in tandem configuration. In Proceedings of the 2021 AIAA Aviation Forum, Virtual Event, 2–6 August 2021. [CrossRef]
12. Jamaluddin, N.S.; Celik, A.; Baskaran, K.; Rezgui, D.; Azarpeyvand, M. Experimental Characterisation of Small-Scaled Propeller-Wing Interaction Noise. In Proceedings of the 28th AIAA/CEAS Aeroacoustics 2022 Conference, Southampton, UK, 14–17 June 2022. [CrossRef]
13. Baskaran, K.; Celik, A.; Jamaluddin, N.S.; Rezgui, D.; Azarpeyvand, M. Aerodynamic and aeroacoustic characteristics of different pitch propellers. In Proceedings of the 28th AIAA/CEAS Aeroacoustics 2022 Conference, Southampton, UK, 14–17 June 2022. [CrossRef]
14. Baskaran, K.; Jamaluddin, N.S.; Celik, A.; Rezgui, D.; Azarpeyvand, M. Aerodynamic and aeroacoustic characteristics of propellers with different blade numbers. In Proceedings of the 28th AIAA/CEAS Aeroacoustics 2022 Conference, Southampton, UK, 14–17 June 2022. [CrossRef]
15. Goldschmidt, J.; Tingle, H.; Ifgu, P.G.; Miller, S.A.; Ukeiley, L.S.; Goldman, B.; Droandi, G.; Lee, K. Acoustics and forces from an isolated rotor system. In Proceedings of the AIAA Scitech 2022 Forum, San Diego, CA, USA, 3–7 January 2022. [CrossRef]
16. Emeis, S.; Baumann-Stanzer, K.; Piringer, M.; Kallistratova, M.; Kouznetsov, R.; Yuhkov, V. Wind and turbulence in the urban boundary layer—Analysis from acoustic remote sensing data and fit to analytical relations. *Meteorol. Z.* **2007**, *16*, 393–406. [CrossRef] [PubMed]
17. Schmitz, F.; Yu, Y. Helicopter impulsive noise: Theoretical and experimental status. *J. Sound Vib.* **1986**, *109*, 361–422. [CrossRef]

18. Deters, R.W.; Ananda Krishnan, G.K.; Selig, M.S. Reynolds number effects on the performance of small-scale propellers. In Proceedings of the 32nd AIAA Applied Aerodynamics Conference, Atlanta, GA, USA, 16–20 June 2014. [CrossRef]

19. Kurtz, D.; Marte, J. *A Review of Aerodynamic Noise from Propellers, Rotors, and Lift Fans*; Technical Report 32-7462; NASA Jet Propulsion Laboratory: La Cañada Flintridge, CA, USA, 1970.

20. Wu, J.; Stalnov, O.; Chen, W.; Yang, Z.; Huang, X. Transient analysis of blade-vortex interaction noise. *Aerosp. Sci. Technol.* **2022**, *120*, 107294. [CrossRef]

21. Yu, Y.H. Rotor blade–vortex interaction noise. *Prog. Aerosp. Sci.* **2000**, *36*, 97–115. [CrossRef]

22. Scharpf, D.F.; Mueller, T.J. An experimental investigation of the sources of propeller noise due to the ingestion of turbulence at low speeds. *Exp. Fluids* **1995**, *18*, 277–287. [CrossRef]

23. Sevik, M. Sound radiation from a subsonic rotor subjected to turbulence. *Fluid Mech. Acoust. Des. Turbomach. Part II* **1974**, *304*, 493–511.

24. Diaz, P.V.; Yoon, S. High-Fidelity Computational Aerodynamics of Multi-Rotor Unmanned Aerial Vehicles. In Proceedings of the 2018 AIAA Aerospace Sciences Meeting, Kissimmee, FL, USA, 8–12 January 2018. [CrossRef]

25. Garrick, I.E.; Watkins, C.E. *A Theoretical Study of the Effect of Forward Speed on the Free-Space Sound-Pressure Field Around Propellers*; Technical Report; NASA Langley Research Center: Hampton, VA, USA, 1953.

26. Hubbard, H.H. Noise Sources. In *Aeroacoustics of Flight Vehicles: Theory and Practice*; Technical Report; National Aeronautics and Space Admin Langley Research Center: Hampton, VA, USA, 1991; Volume 1.

27. Mayer, Y.; Jawahar, H.K.; Szoke, M.; Azarpeyvand, M. Design of an aeroacoustic wind tunnel facility at the University of Bristol. In Proceedings of the 24th AIAA/CEAS Aeroacoustics Conference, Atlanta, GA, USA, 25–29 June 2018. [CrossRef]

28. Abdallah, M.N.; Sarkar, T.K.; Salazar-Palma, M. Far field's starting distance. In Proceedings of the 2016 International Conference on Electromagnetics in Advanced Applications (ICEAA), Cairns, Australia, 19–23 September 2016; pp. 789–792. [CrossRef]

29. Bowen, L.; Celik, A.; Azarpeyvand, M.; da Silva, C.R.I. Grid generated turbulence for aeroacoustic facility. *AIAA J.* **2021**, *60*, 1–15. [CrossRef]

30. Anderson, J.M.; Catlett, M.R.; Stewart, D. Modeling rotor unsteady forces and sound due to homogeneous turbulence ingestion. *AIAA J.* **2015**, *53*, 81–92. [CrossRef]

31. Wright, S. The acoustic spectrum of axial flow machines. *J. Sound Vib.* **1976**, *45*, 165–223. [CrossRef]

32. Baars, W.J.; Bullard, L.; Mohamed, A. Quantifying modulation in the acoustic field of a small-scale rotor using bispectral analysis. In Proceedings of the AIAA Scitech 2021 Forum, Virtual Event, 11–15 & 19–21 January 2021. [CrossRef]

33. Liu, W.; Zagzebski, J.A.; Liu, W. Trade-offs in data acquisition and processing parameters for backscatter and scatterer size estimations. *IEEE Trans. Ultrason. Ferroelectr. Freq. Control.* **2010**, *57*, 340–352. [CrossRef] [PubMed]

34. Qi, H.; Wang, P.; Jiang, L.; Zhang, Y. Investigation on aerodynamic noise characteristics of coaxial rotor in hover. *Appl. Sci.* **2022**, *12*, 2813. [CrossRef]